Ce1−x Co x O2 Nanorods Prepared by Microwave-Assisted Hydrothermal Method: Novel Catalysts for Removal of Volatile Organic Compounds

Article *in* Science of Advanced Materials · July 2015

DOI: 10.1166/sam.2015.2059

CITATIONS
3

READS
149

9 authors, including:

Luiz F. D. Probst
Federal University of Santa Catarina
72 PUBLICATIONS **1,063** CITATIONS
SEE PROFILE

Andres Cantarero
University of Valencia
325 PUBLICATIONS **4,290** CITATIONS
SEE PROFILE

Mauricio M. de Lima, Jr.
University of Valencia
68 PUBLICATIONS **849** CITATIONS
SEE PROFILE

Vinícius D. Araújo
Universidade Federal Rural de Pernambuco
31 PUBLICATIONS **371** CITATIONS
SEE PROFILE

AMERICAN SCIENTIFIC PUBLISHERS

Science of Advanced Materials
Vol. 6, pp. 1–9, 2014
(www.aspbs.com/sam)

ARTICLE

$Ce_{1-x}Co_xO_2$ Nanorods Prepared by Microwave-Assisted Hydrothermal Method: Novel Catalysts for Removal of Volatile Organic Compounds

Rosana Balzer[1,*], Luiz F. D. Probst[1], Andrés Cantarero[2], Maurício M. de Lima Jr[2,3], Vinícius D. Araújo[4], Maria I. B. Bernardi[4], Waldir Avansi Jr[5], Raul Arenal[6,7], and Humberto V. Fajardo[8]

[1]*Departamento de Química, Universidade Federal de Santa Catarina, UFSC, 88040-900, Florianópolis–SC, Brasil*
[2]*Instituto de Ciencia de los Materiales, Universidad de Valencia, E-46071 Valencia, Spain*
[3]*Fundación General, Universitat de Valencia, Valencia, Spain*
[4]*Instituto de Física de São Carlos, Universidade de São Paulo, USP, 13560-970, São Carlos–SP, Brasil*
[5]*Departamento de Física, Universidade Federal de São Carlos, UFSCar, 13565-905, São Carlos–SP, Brasil*
[6]*Laboratorio de Microscopias Avanzadas (LMA), Instituto de Nanociencia de Aragon (INA), Universidad de Zaragoza, Calle Mariano Esquillor, 50018 Zaragoza, Spain*
[7]*ARAID Fundation, Calle Mariano de Luna, 50018 Zaragoza, Spain*
[8]*Departamento de Química, Universidade Federal de Ouro Preto, UFOP, 35400-000, Ouro Preto–MG, Brasil*

ABSTRACT

In this study, nanorods of a $Ce_{1-x}Co_xO_2$ system, with $x = 0$, 0.05, 0.10, 0.15 and 0.20, were synthesized employing a microwave-assisted hydrothermal method and their catalytic activity in the total oxidation of three VOCs (benzene, toluene and *o*-xylene) was investigated. The physicochemical characterization showed that the inclusion of cobalt led to an increase in the oxygen vacancies in the system. Also, an increase in the catalytic activity was observed with the progressive incorporation of cobalt into the ceria matrix. The results revealed that the $Ce_{0.80}Co_{0.20}O_2$ catalyst was able to remove 100% of the benzene, nearly 100% of the toluene and around 70% of the *o*-xylene. Increasing the amount of oxygen vacancies could result in an enhancement of the bulk and surface oxygen mobility. The higher oxidation activity observed for the catalyst with the highest cobalt load can be attributed to a combination of several factors, including a greater number of active sites of the cobalt being exposed and greater mobility of the active oxygen species.

KEYWORDS: Hydrothermal Method, Nanorods, Catalytic Oxidation, Volatile Organic Compounds.

1. INTRODUCTION

Volatile organic compounds (VOCs) are hazardous highly toxic pollutants that cause a number of environmental and human health problems. They are released during a wide range of industrial, transportation and commercial activities and their emissions have reached high levels.[1–3] Several VOCs removal techniques, including physical, chemical and biological methods, have been described in the literature. Catalytic oxidation has been acknowledged as the most effective approach, mainly due to its high degradation efficiency, low energy cost, the potential for the removal of low concentrations of VOCs and the low thermal NO_x emissions involved.[2,4–6] The noble metal-based catalysts used in this process frequently exhibit better performance when compared to non-noble metal-based catalysts.[3,5,7–9] However, due to the high cost of the noble metals, which can represent an economic obstacle to the employing the process, these are increasingly being replaced with cheaper catalysts employing transition metals.[7,10] Of the metal oxides, cobalt and cerium oxides have been shown to be among the most efficient for the promotion of oxidation reactions.[10,11] To be an active catalyst for VOCs oxidation, cobalt must be well dispersed on the support and highly reducible particles. This can be achieved by using a suitable support. The use of ceria as support offers some advantages due to its redox property which can help the dispersion of the supported metal and ensure

*Author to whom correspondence should be addressed.
Email: rosanabalzer@gmail.com
Received: XX Xxxx XX
Accepted: XX Xxxx XX

more oxygen available for the oxidation reaction.[12–15] Thus, aiming to contribute to the development of non-noble metal-based catalysts to be applied in processes involving oxidation reactions of VOCs, the objective of this study was to investigate the use of well designed bifunctional catalysts, based on cobalt and cerium, for the total oxidation of volatile organic compounds (benzene, toluene and *o*-xylene), which were chosen as model compounds due to their toxic, carcinogenic and molecular characteristics. The $Ce_{1-x}Co_xO_2$ catalysts were prepared through the microwave-assisted hydrothermal method. This method combines the advantages of both hydrothermal and microwave-irradiation techniques. Recently, this procedure has attracted the attention of researchers since it offers very short reaction times (e.g.,: Ifrah et al.[16] synthesized $La_{1-x}Ag_xMnO_{3+\delta}$ during 24 hours in a conventional hydrothermal method while only 120 minutes was necessary for the microwave-assisted method.), the production of small particles with a narrow particle size distribution and high purity, applicability to samples with different morphologies and structures, and low energy consumption compared with conventional methods.[17–19]

Differences in the activity exhibited by the catalysts have been attributed to their physical and chemical properties (such as specific surface area, morphology, size, dispersion and strength of interaction between metal particle and support) which are related to the method used for their preparation. The importance of these properties is confirmed by the large number of publications dealing specifically with the synthesis of nanostructured materials for catalytic applications. Compared with the traditional bulk catalysts, the nanostructured catalysts have many improvements concerning the structural aspects, which are expected to contribute to enhance the catalytic activity due to their unique properties. The use of particles in a nanometer scale increases the relative proportion of active sites per unit area of the metal particles, resulting in a large surface area for contact between the catalyst active phase and the reactant molecules. This means that more reactions can occur, and thus a more efficient catalyst can be expected.[20,21] In this regard, the development of nanostructured catalysts which exhibit superior activity in the catalytic oxidation process is an important challenge confronting researchers. To the best of our knowledge, this is the first time that $Ce_{1-x}Co_xO_2$ nanorods, synthesized via microwave-assisted hydrothermal method, is used as catalysts for the total oxidation of benzene, toluene and *o*-xylene.

2. EXPERIMENTAL DETAILS

2.1. Catalyst Preparation

In a typical procedure to obtain $Ce_{1-x}Co_xO_2$ ($x = 0$, 0.05, 0.10, 0.15 and 0.20) nanostructures, 0.02 mol of the precursors cerium chloride ($CeCl_3 \cdot 7H_2O$-Sigma-Aldrich) and cobalt chloride ($CoCl_2 \cdot 6H_2O$-Sigma-Aldrich) were dissolved in 50 mL of distilled water. In the next step, 50 ml of a 10 M NaOH solution was added rapidly under vigorous stirring. The mixed solution was placed in a 110 mL Teflon autoclave (filling 90% of its volume) which was sealed and placed in a microwave assisted hydrothermal system, applying 2.45 GHz of microwave radiation at a maximum power of 800 W. The temperature was measured with a temperature sensor (type K thermocouple) inserted inside the vessel. The as-prepared solution was subjected to microwave hydrothermal synthesis with heating to a temperature of 140 °C in 1 min, which was held for 10 min. The sample was then air-cooled to room temperature. The as-obtained precipitate powder was washed several times with distilled water and isopropyl alcohol and then dried on a hot plate at 60 °C for 24 h. The resulting powder was then calcined at 600 °C for 2 h.

2.2. Catalyst Characterization

The specific surface area (BET method) was estimated from the N_2 adsorption/desorption isotherms at liquid nitrogen temperature, using a Micromeritics ASAP 2000. The equivalent spherical diameter of the particles, d_{BET}, was calculated with the equation, $d_{BET} = 6/(S_s\rho)$, where S_s is the specific surface area and ρ is the density of the material in the particles.

The powders were characterized structurally in an X-ray diffractometer (Rigaku, Rotaflex RU200B) with CuKα radiation (50 kV, 100 mA, $\lambda = 1.5405$ Å), using a θ–2θ configuration and a graphite monochromator. The scanning range was between 20 and 90° (2θ), with a step size of 0.02° and a step time of 5.0 s. Rietveld analysis was performed using the Rietveld refinement program GSAS.[22] A pseudo-Voigt profile function was used.

Elemental analysis of the catalysts was performed using a Varian AA240FS atomic absorption spectrometer in order to verify their doping levels.

Raman spectroscopy was carried out at room temperature in a Jobin-Yvon-T64000 micro-Raman system in the backscattering geometry, using different laser line excitations (325, 364, 457, 488, 514 and 647 nm). We used an optical lens with 100X magnification, which supplies an average laser spot size of 1 μm.

Photoluminescence measurements were carried out in a McPherson—207 monochromator, with 1200 gr/mm gratings equipped with an Andor CCD. The samples were mounted in a closed-cycle Leybold cryostat, which allowed a temperature of 7 K. The 325 nm excitation wavelength of a He–Cd laser (Kimmon Koha) was used, with the nominal output power kept at 5 mW and a spot size of approximately 100 μm in diameter.

The different morphologies of the nanocatalysts were determined by field emission scanning electron microscopy (FE-SEM) using a Zeiss Supra™ 35 FE-SEM microscope and also investigated by transmission electron microscopy (TEM) performed on a JEM 2100 URP (operating at 200 KV) and on an imaging-side aberration-corrected FEI Titan-Cube microscope working at 300 kV,

equipped with a Cs corrector (CETCOR from CEOS GmbH).

The Electron paramagnetic resonance (EPR) spectra were recorded at 20 K in an X-band Bruker ELEXSYS E580 spectrometer. The temperature was controlled by an Oxford ITC503 cryogenic system. The spectra were obtained at a modulation frequency of 100 kHz, modulation amplitude of 0.2 mT and microwave power of 1 mW.

The O_2-chemisorption measurements were conducted at 600 °C using a ChemBET analyzer (Quantachrome Instruments).

2.3. Catalytic Tests

The catalytic activity was measured in a fixed bed tubular quartz reactor (39.5 cm length and 9 mm inner diameter) under atmospheric pressure. The following conditions were chosen: catalyst volume 0.11 g, inlet benzene (Vetec®) concentration 1.2 $g \cdot m^{-3}$, toluene (Vetec®) concentration 0.7 $g \cdot m^{-3}$, *o*-xylene (Vetec®) concentration 0.5 $g \cdot m^{-3}$ in air, gas flow rate 20 $cm^3 \cdot min^{-1}$, residence time 0.3 s, gas hourly space velocity 12000 h^{-1} and temperature range 150–750 °C. The reaction data were collected after at least 2 h on-stream at room temperature. The reaction products were determined by GC-MS. The reactant and product mixtures were analyzed using two on-line gas chromatographs equipped with FID and TCD detector and an HP-5 column. The catalytic activity was expressed as the degree of the conversion of benzene, toluene and *o*-xylene, respectively. The conversion of the BTX compounds (benzene, toluene and *o*-xylene) was calculated as follows:

$$\text{BTXs } (\%) = \frac{[\text{BTXs}]_{\text{in}} - [\text{BTXs}]_{\text{out}}}{[\text{BTXs}]_{\text{in}}} \times 100\%$$

where BTXs (%) = percentage of BTX conversion; $[\text{BTXs}]_{\text{in}}$ = input quantity and $[\text{BTXs}]_{\text{out}}$ = output quantity.

3. RESULTS AND DISCUSSION

Table I shows the BET specific surface area of the catalysts and the density and the equivalent spherical diameter of the particles. The specific surface area of the catalysts (S_s) varied monotonically with the composition. A linear decrease in the surface area with increasing cobalt content was observed. The behavior of the equivalent spherical diameter of the particles (d_{eq}) was the inverse of that observed for the specific surface area, indicating an increase in particle size with increasing cobalt content. It has been shown that an increase in the size of CeO_2 nanostructures prepared by the microwave-assisted hydrothermal method can be described by the process of Ostwald ripening coupled with self-assembly.[23, 24] For materials prepared under the same time/temperature conditions, the only factors influencing the growth of the particles are the diffusion coefficient and the surface energy. The solubilization of a lower valence dopant in ceria leads to the formation of oxygen vacancies and, as a consequence, an increase in the self-diffusion coefficient, resulting in larger particles than in pristine material (smaller surface area).[25] Hence, the reduction in the specific surface area of the samples containing cobalt can be attributed to substitution of the Ce^{4+} ion by Co^{2+} and/or Co^{3+}, which generates an increase in the mole fraction of oxygen vacancy, maintaining charge neutrality and, consequently promoting an increase in the diffusion coefficient resulting in the growth of the nanoparticles.

Figure 1 shows the XRD patterns for the $Ce_{1-x}Co_xO_2$ samples. Fluorite-type cubic CeO_2 with F m -3 m space group (ICSD no. 156250 or JCPDS no. 43-1002) was present in all samples. Cubic Co_3O_4 peaks (ICSD no. 69366 or JCPDS no. 01-080-1533) were detected in all samples containing cobalt. Table I describes the lattice parameter (a) and the oxygen occupancy factor (O_{occup}) calculated from the Rietveld refinement and the R_{exp} and R_{Bragg} quality factors of the refinement. The crystallite size values of all samples were evaluated using Scherrer's equation.[26] The average crystallite size was calculated using the full width at half maximum of (1 1 1) peaks from the XRD patterns. The lattice parameter did not vary with the composition despite the smaller Co^{2+} ion (radii = 0.90 Å) or Co^{3+} ion (radii = 0.61 Å) substituting the larger Ce^{4+} ion (radii = 0.97 Å).[27, 28] Also, the samples presented small crystallite sizes (11 nm) that do not vary with composition. A decrease in oxygen occupancy occurs with increasing cobalt content, which is related to an increase in the amount of oxygen vacancies in the ceria matrix, preserving electron neutrality as Ce^{4+} ions are substituted by Co^{2+} and/or Co^{3+}, which could cause an increase in the lattice parameter due to strains created by the oxygen

Table I. Specific surface area (S_s), lattice parameter (a), crystallite size (D_{cryst}), oxygen occupancy factor (O_{ocup}), density (ρ), equivalent spherical diameter (d_{eq}) and oxygen storage capacity (OSC) of $Ce_{(1-x)}Co_{(x)}O_2$ nanoparticles.

Sample	S_s (m^2/g)	a (Å)[1]	D_{cryst} (nm)	O_{occup}	ρ (g/cm^3)[1]	d_{eq} (nm)	R_{exp} (%)	R_{Bragg} (%)	OSC ($mmol/m^2$)
CeO_2	82.1	5.4176 ± 0.0001	11	0.954 ± 0.007	7.128	10	6.88	3.42	–
$Ce_{0.95}Co_{0.05}O_2$	81.9	5.4157 ± 0.0001	11	0.914 ± 0.006	6.914	11	6.81	3.78	3.02
$Ce_{0.90}Co_{0.10}O_2$	77.8	5.4161 ± 0.0001	10	0.885 ± 0.006	6.704	12	6.83	4.07	3.96
$Ce_{0.85}Co_{0.15}O_2$	72.8	5.4161 ± 0.0001	11	0.887 ± 0.006	6.531	13	6.86	3.15	4.51
$Ce_{0.80}Co_{0.20}O_2$	65.7	5.4158 ± 0.0001	11	0.851 ± 0.006	6.336	14	7.04	3.97	4.96

Note: [1]Calculated via Rietveld refinement.

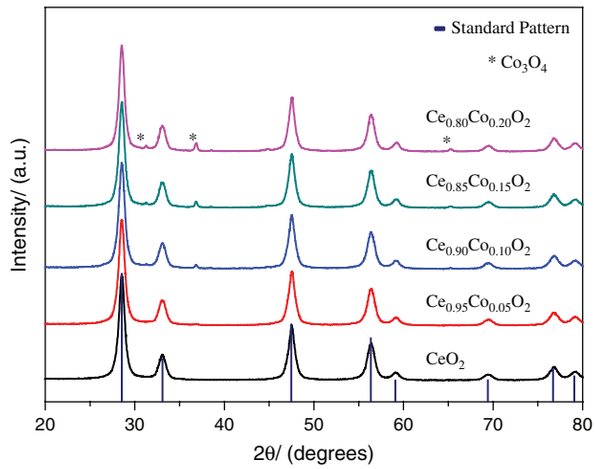

Fig. 1. XRD patterns obtained for $Ce_{1-x}Co_xO_2$ catalysts.

vacancies formed.[29] These results suggest that the effect of the oxygen vacancy increase compensates the negative substitution effect. Also, cobalt most likely resides on the surface of the ceria and as the cobalt content increases Co_3O_4 precipitates could be formed.[30]

Figure 2(a) shows the Raman spectra (excitation line 457 nm) for the samples. Dioxides with a fluorite structure have only one allowed Raman mode, which has an F_{2g} symmetry and can be viewed as a symmetric breathing mode of the O atoms around each cation. In bulk CeO_2 this frequency is 465 cm^{-1}. We observed two main features centered at 462 and 600 cm^{-1}. The former is assigned to the fluorite F_{2g} mode, confirming the XRD results. The broad band at around 600 cm^{-1} can be ascribed to oxygen vacancies and defects caused by small-size effects.[31] As the cobalt content increases, the F_{2g} mode peak shifts to lower frequencies and becomes broader and asymmetric (confirmed by a simple Lorentz fit shown in the inset in Fig. 2(a)), while the mode around 600 cm^{-1} becomes more intense with increasing cobalt content. According to Spanier et al.[29] several factors can contribute to the changes in the Raman peak position and line width of the F_{2g} mode, such as phonon confinement, strain, broadening associated with the size distribution, defects and variations in phonon relaxation with particle size. Our results suggest that the insertion of cobalt in the ceria matrix may induce strain and defects (as seen in XRD results), leading to changes in the F_{2g} mode frequency.

For the samples containing cobalt, three peaks at around 483, 525 and 693 cm^{-1} were observed and these are ascribed to vibrational modes of Co_3O_4.[32] Figure 2(b) shows Raman spectra with different excitation lines of the $Ce_{0.80}Co_{0.20}O_2$ sample. According to Popovic et al.,[33] due to the higher concentration of vacancies followed by an accumulation of a stronger charge in the surface layers than in the bulk of CeO_2 nanocrystalline samples, changes in the Raman spectra using various excitation energies are expected, since the laser light penetration depth is

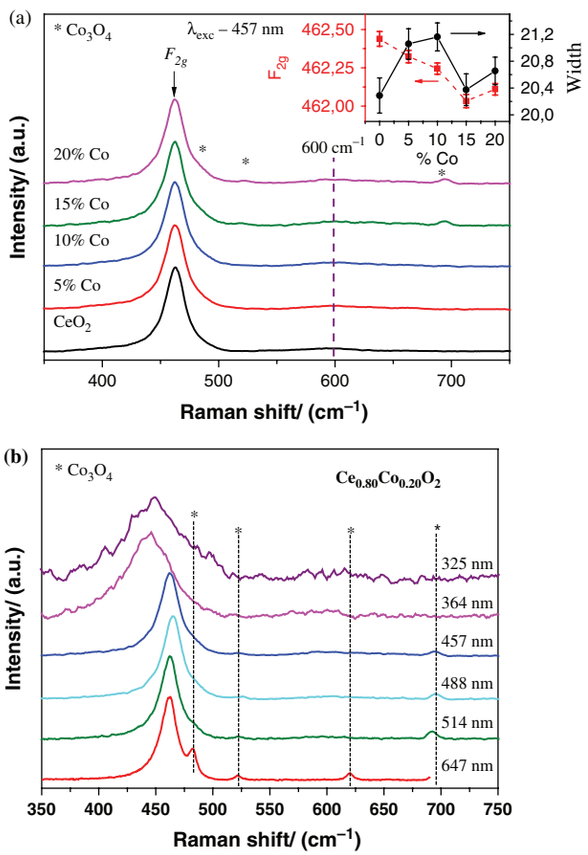

Fig. 2. (a) Raman spectra (excitation line 457 nm) for $Ce_{1-x}Co_xO_2$ nanoparticles; (b) Raman spectra using different excitation lines for $Ce_{0.80}Co_{0.20}O_2$ sample. The inset shows the frequency shift and broadening of the F_{2g} mode peak.

dependent on the incident light wavelength and absorption coefficient of the sample. They showed that higher excitation energy provides information related to the surface properties rather than those of the bulk of the nanocrystal. The F_{2g} mode peak was shifted to lower frequencies and became broader with increasing excitation energy, indicating a higher concentration of defects and greater accumulation of charge on the surface of the sample. Nevertheless, a resonant effect should not be ruled out in order to explain the strong shift in the spectra when excited with 325 and 364 nm. Also, peaks related to Co_3O_4 became more pronounced with decreasing excitation energy, indicating a higher concentration of Co_3O_4 in the bulk than on the surface of the nanoparticles.

Figure 3 shows the photoluminescence spectra of the samples obtained at 7 K with an excitation wavelength of 325 nm. A simple Gaussian fit for pure CeO_2 is also shown (dashed curves). The samples could emit visible light showing a PL with a broad band that could be fitted with two Gaussians functions centered at approximately 595 and 687 nm. The broad band observed for the samples is attributed to sub-band transitions within

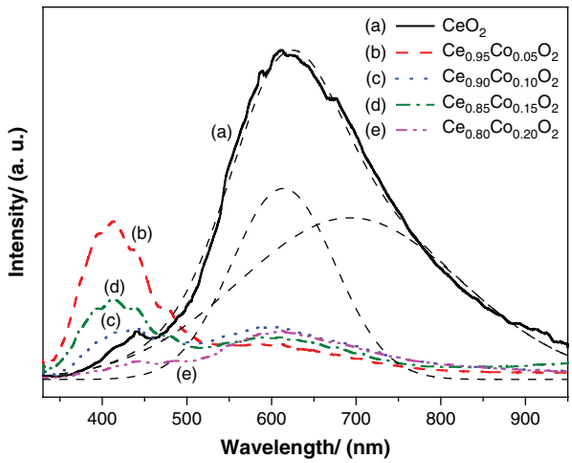

Fig. 3. Photoluminescence spectra obtained at 7 K with an excitation wavelength of 325 nm for the different catalysts. The dashed lines show the profiles for the Gaussian fits for the CeO_2 sample.

the band gap, which are closely related to surface defects and oxygen vacancies, as previously noted for various nanomaterials.[34–37] The samples with cobalt also presented a peak at around 410 nm related to the hopping from different defect levels to the O 2p band.[38] The spectra for the samples are blue-shifted in comparison with the spectrum for the pure CeO_2. Also, in contrast with the pure ceria, for the samples with cobalt, the contribution of the 595 nm band was more pronounced than that of the 687 nm band, since the substitution of Ce^{4+} by Co^{2+} or Co^{3+} induces an increase in the oxygen vacancy concentration (as shown by the XRD and Raman measurements). Thus, it can be assumed that the contribution of the band at around 595 nm is related to oxygen vacancies while that at around 687 nm is related to surface defects. Finally, the intensity of the band at around 410 nm is inversely related to the oxygen vacancies, i.e., the oxygen vacancies increase and the band at around 410 nm becomes less intense with increasing cobalt content.

Figure 4 shows the FE-SEM images of the $Ce_{1-x}Co_xO_2$ nanoparticles. The samples are composed mainly of nanorods with an average diameter of 10 nm and a length of 100 nm. The morphology of the as-obtained samples was verified by TEM analysis (Fig. 5). As observed from the FE-SEM analysis, no significant differences in the morphologies of the $Ce_{1-x}Co_xO_2$ nanoparticles were observed. Therefore, only the images for the CeO_2 and $Ce_{0.80}Co_{0.20}O_2$ samples are shown by way of example. In Figures 5(a) and (b) it is clear that despite the presence of cobalt ions no significant change can be observed, the $Ce_{1-x}Co_xO_2$ ($x = 0$ and 0.20) samples being comprised of wide rods of around 10 nm. The same morphology was observed for pristine CeO_2 obtained by the same synthesis route in a previous paper of our research group,[24] where it was demonstrate that the morphology of the CeO_2 anisotropic nanostructure is governed by the oriented attachment (OA) growth mechanism.[39] It is interesting to note that the morphology of the samples in this study is not affected by the cobalt content. Further and more precise HRTEM analyses of the $Ce_{0.80}Co_{0.20}O_2$ sample confirmed these findings. As a matter of fact, the HRTEM micrograph displayed in Figure 5(c) as well as its corresponding Fourier transform (FFT, Fig. 5(d)), show that the addition of different amounts of Co ions in the CeO_2 structure do not affect the single-crystalline nature of its structure.

The EPR spectra of the $Ce_{1-x}Co_xO_2$ samples are presented in Figure 6. A broad resonance at $g_{eff} \sim 5.4$ and two peaks at $g_{eff} = 4.8$ and $g_{eff} = 1.95$ are observed. The feature at $g_{eff} \sim 5.4$ and the peak at $g_{eff} = 4.8$ are related to different Co^{2+} species, which in our samples are more likely to be Co^{2+} substituting Ce^{4+}/Ce^{3+} in the cerium matrix and Co^{2+} present in Co_3O_4 precipitates (as seen from XRD results).[40–46] The peak at $g_{eff} = 1.95$ is related to Ce^{3+} species.[46] According to Figure 6(b), a decrease in the intensity of the peak related to Ce^{3+} species is observed with increasing cobalt content, indicating that Ce^{3+} are most likely to be substituted by the non-paramagnetic ion Co^{3+}.

The results obtained from the oxygen chemisorption measurements are shown in Table I. The oxygen storage capacity (OSC) for each sample was calculated based on the oxygen uptake. These values allow us to estimate the total amount of oxygen available in the oxide catalyst.[47] As the cobalt content increased the oxygen uptake also increased. The $Ce_{0.80}Co_{0.20}O_2$ sample presented the largest OSC, indicating that this sample has a higher amount of oxygen vacancies. The creation of oxygen vacancies due to the incorporation of cobalt enhanced the oxygen mobility in the $Ce_{1-x}Co_xO_2$ nanorods, as also indicated by the characterization results discussed above.

In order to investigate the catalytic activity of the synthesized $Ce_{1-x}Co_xO_2$ nanorods, benzene, toluene and *o*-xylene (BTX) oxidation reactions were carried out. The only reaction products detected in the experiments were H_2O and CO_2. Figure 7 shows the BTX conversion for all catalysts as a function of reaction temperature. Table II shows the light-off temperature (T_{50}) for BTX oxidation promoted by the $Ce_{1-x}Co_xO_2$ catalysts. It can be observed from the results that the $Ce_{1-x}Co_xO_2$ nanorods were active in the reactions studied and showed a similar tendency, the BTX conversion increasing with an increase in the reaction temperature, as expected. The progressive incorporation of cobalt to the ceria matrix causes an increase in the catalytic activity. The order of catalytic activity in the BTX oxidation reactions was as follows: $Ce_{0.80}Co_{0.20}O_2 > Ce_{0.85}Co_{0.15}O_2 > Ce_{0.90}Co_{0.10}O_2 > Ce_{0.85}Co_{0.05}O_2$. In the case of benzene, for example, T_{50} was observed at 156 °C over $Ce_{0.80}Co_{0.20}O_2$, whereas this value increased to 172 °C over $Ce_{0.85}Co_{0.15}O_2$, to 183 °C over $Ce_{0.90}Co_{0.10}O_2$ and to 216 °C over $Ce_{0.95}Co_{0.05}O_2$, verifying the superior activity

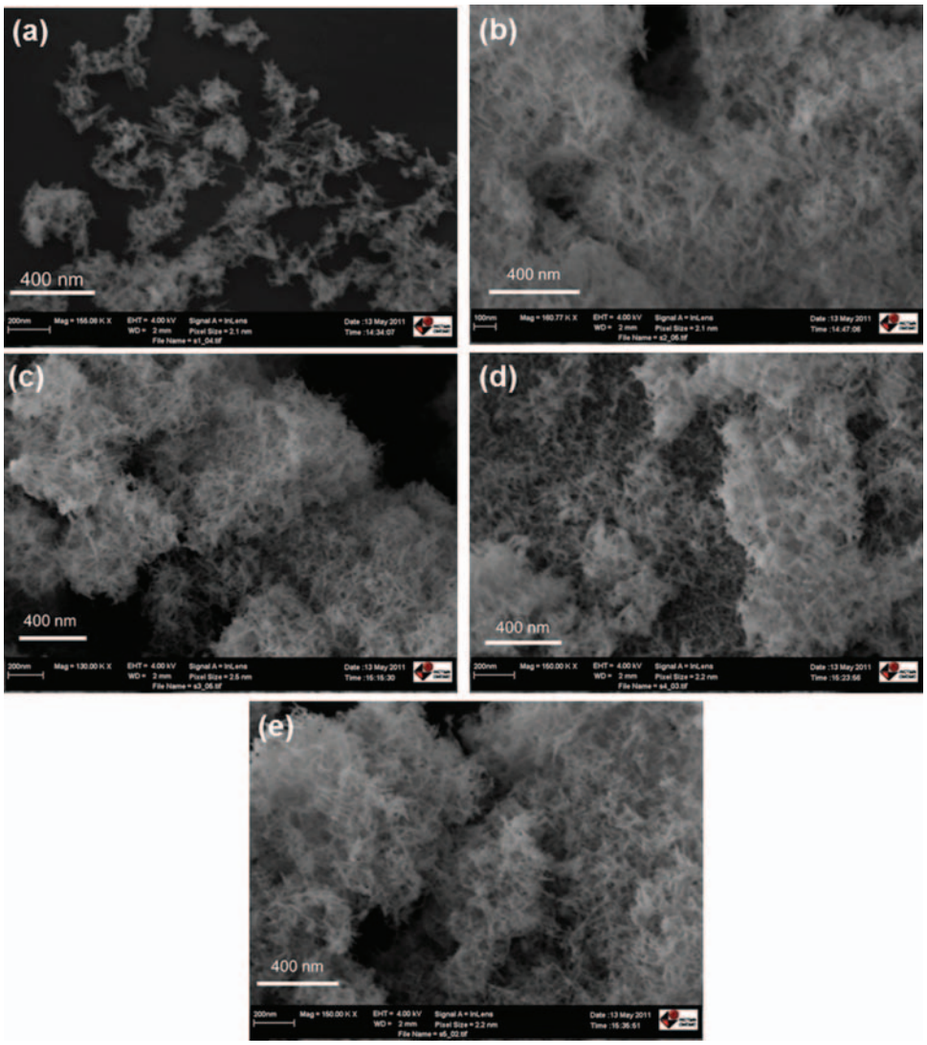

Fig. 4. FE-SEM images of the samples: (a) CeO_2, (b) $Ce_{0.95}Co_{0.05}O_2$, (c) $Ce_{0.90}Co_{0.10}O_2$, (d) $Ce_{0.85}Co_{0.15}O_2$, (e) $Ce_{0.80}Co_{0.20}O_2$.

of the catalyst with the highest cobalt content. Catalytic oxidation can be greatly influenced by the nature of the reactant. So, different activities can be expected for the different organic compounds at the same reaction condition. The oxidation of benzene gave the lowest light-off temperature, followed by toluene and *o*-xylene. In the case of benzene it was possible to achieve complete conversion (over $Ce_{0.80}Co_{0.20}O_2$ catalyst, 100% of benzene was transformed at about 700 °C) but in the case of toluene and *o*-xylene this was not possible. It has been previously noticed that when aromatic compounds are associated with the methyl groups they are not as easily oxidized as benzene.[48]

It is clear from the data in Table II that the lowest light-off temperatures were observed for the $Ce_{0.80}Co_{0.20}O_2$ catalyst, even though this catalyst had the lowest specific surface area. The specific surface area decreased with an increase in the cobalt content and this did not appear to influence the fact that $Ce_{0.80}Co_{0.20}O_2$ was the catalyst that presented the highest activity. This tendency toward higher activity can be attributed to the physicochemical properties of the catalysts, which varied according to the cobalt content. Increasing the cobalt concentration in the catalyst (Ce^{4+} ions are substituted by Co^{2+} and/or Co^{3+} ions and Ce^{3+} ions substituted by Co^{3+}, as indicated by XRD and EPR results) leads to a higher number of active sites being available for the oxidation reactions, considering that cobalt is the most active species in the oxidation reactions, which results in higher conversion levels.[49–53] In the presence of the cobalt species, the reduction of Ce^{+4}/Ce^{+3} is promoted and this factor is favorable for the oxidation of hydrocarbons. Ceria can provide oxygen to cobalt (reducing agent), which retains its higher valence state, with increasing cobalt loading. This effect of ceria contributing to maintaining the high valence state of cobalt species improves the catalytic activity in oxidation reactions.[44, 52, 54] Another factor to be considered is the presence of oxygen vacancies on the catalyst surface, as confirmed by the characterization results discussed

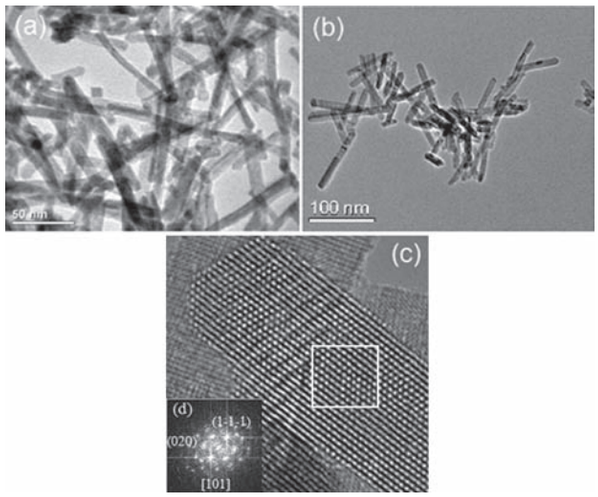

Fig. 5. TEM images of the samples: (a) CeO_2 and (b) $Ce_{0.80}Co_{0.20}O_2$; (c) and (d) HRTEM image and its fast Fourier transform (FFT) of the $Ce_{0.80}Co_{0.20}O_2$ sample, respectively.

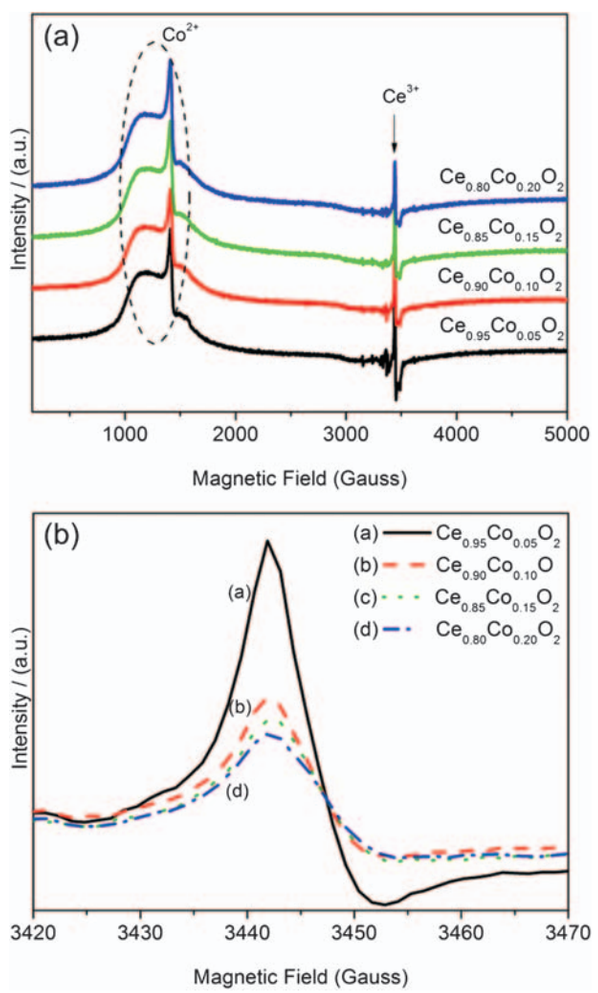

Fig. 6. (a) EPR spectra of the catalysts and (b) enlarged view of the peak related to Ce^{3+} species.

above, which is of importance in relation to the oxidation of hydrocarbons. An increase in the amount of oxygen vacancies could result in an enhancement of the bulk and surface oxygen mobility, factors which are thought to play an important role in oxidation reactions. It has been previously verified that the introduction of a metal ion

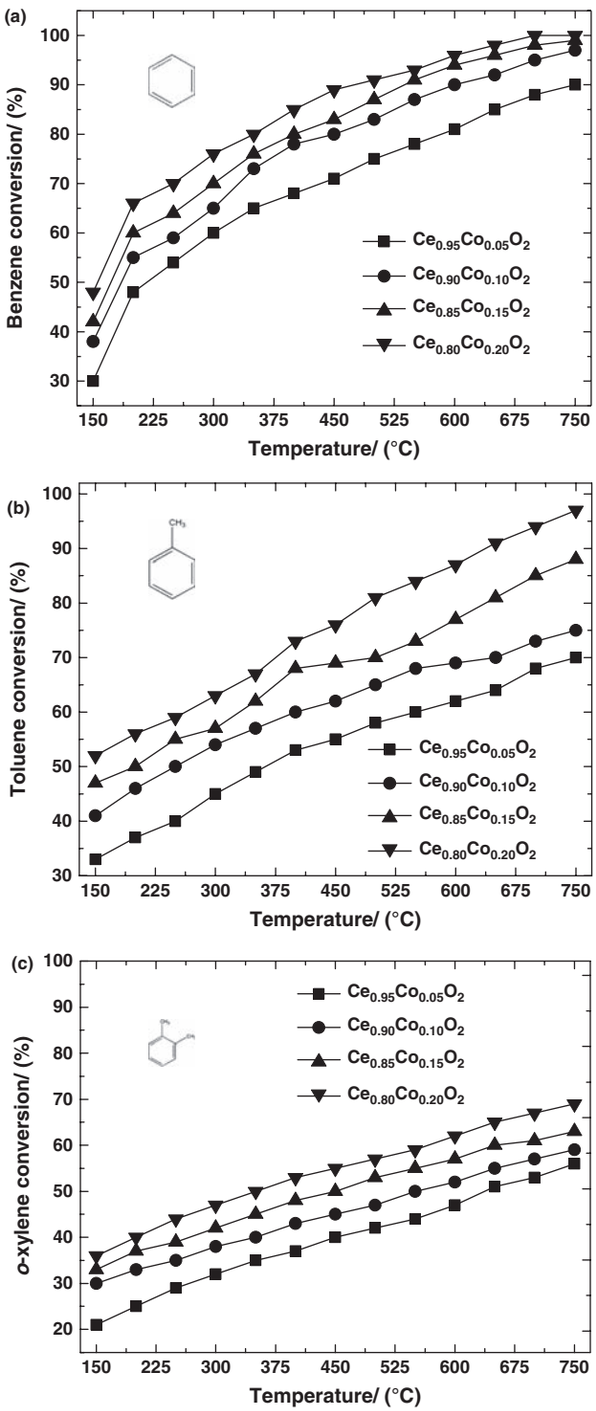

Fig. 7. Conversion of VOCs as a function of the reaction temperature for the $Ce_{(1-x)}Co_{(x)}O_2$ catalysts: (a) benzene, (b) toluene and (c) *o*-xylene.

ARTICLE

Table II. Temperatures for the 50% VOC conversion (T_{VOC50}) observed for the different catalysts.

Catalyst	$T_{benzene50}$ (°C)	$T_{toluene50}$ (°C)	$T_{o\text{-}xylene50}$ (°C)
$Ce_{0.95}Co_{0.05}O_2$	216	362	268
$Ce_{0.90}Co_{0.10}O_2$	183	250	150
$Ce_{0.85}Co_{0.15}O_2$	172	200	<150
$Ce_{0.80}Co_{0.20}O_2$	156	<150	<150

can further improve the oxygen mobility by increasing the amount of oxygen vacancies on the catalyst surface.[47,55] The higher oxygen mobility promotes the migration of oxygen species across the catalyst structure, resulting in higher oxidation activity.[47,55–59] Oxygen migration across the catalyst surface is essential in oxidation reactions, where the oxidation-reduction cycles determine the activity of the catalyst. It is well known that, when cerium oxide based catalysts are involved, the oxidation of hydrocarbons can proceed via the Mars-van Krevelen mechanism in which the substrate is oxidized by the solid. Thus the key steps are the supply of oxygen by the reducible oxide, the introduction of the oxygen species from the lattice oxide into the substrate molecule, and the re-oxidation of the reduced solid by the oxygen-containing gaseous phase, which is the rate-determining step of the reaction.[7] It is interesting to note in our case that as the cobalt addition increased an increase in oxygen vacancies was observed, which, in turn, increased the oxygen mobility and subsequently the catalytic activity for the oxidation. Lattice oxygen atoms from the surface of the catalyst are consumed by the organic compound adsorbed on its surface and oxygen vacancies are created. These vacancies are filled by the oxygen atoms that diffuse from the bulk to the surface of the catalyst or by di-oxygen in the air stream during the experiments. In addition, it has been postulated that larger amounts of mobile oxygen species will be encountered on oxides which posses more crystalline defects.[56] In the case of the cobalt-doped samples, which have large crystallites, there are more crystalline defects present compared with the pure ceria and hence a larger amount of mobile oxygen species, as revealed by the Raman measurements. Some authors have reported that increasing the oxygen mobility of ceria-based catalysts, by introducing defective sites, seems to effectively promote hydrocarbon oxidation.[56,57,60] These observations may explain the catalytic behavior observed for the $Ce_{1-x}Co_xO_2$ samples.

4. CONCLUSIONS

In this study, $Ce_{1-x}Co_xO_2$ catalysts were successfully synthesized and tested for total BTX oxidation. The microwave-assisted hydrothermal method proved to be efficient for the synthesis of nanorods with sizes of around 10 nm in diameter and 100 nm in length. Rietveld analysis and optical characterization showed that cobalt doping did not change the CeO_2 cubic structure, but the progressive inclusion of cobalt led to an increase in the oxygen vacancies in the system. Also, the optical characterization revealed a higher concentration of structural defects and oxygen vacancies on the surface of the nanorods. The catalytic results clarify that the reaction conditions and the nature of the catalyst influenced the BTX oxidation. The conversion was also found to be dependent on the particular VOC to be oxidized. With the gradual increase of cobalt content to 20%, the active sites increase as well, resulting in the promotion in the oxidation efficiency of the catalysts. The superior performance of the $Ce_{0.80}Co_{0.20}O_2$ catalyst may be due to a combination of several factors, including a higher number of exposed active sites of cobalt and greater oxygen mobility.

Acknowledgments: This research was supported by the Brazilian funding support agencies: FAPESP, CAPES, CNPq, FAPEMIG and the Spanish bilateral project AIB2010SE-00160. The transmission electron microscopy was carried out at LME/LNNano/CNPEM and at the Laboratorio de Microscopias Avanzadas at the Instituto de Nanociencia de Aragon—Universidad de Zaragoza (Spain). R. A. also acknowledges funding from grants 165-119 and 165-120 from U. de Zaragoza and from the ARAID foundation. Part of the research leading to these results has received funding from the European Union Seventh Framework Program under Grant Agreement 312483—ESTEEM2 (Integrated Infrastructure Initiative—I3). The authors are indebted to Professor Dr. Otaciro Rangel and especially to Dr. José Fernando de Lima for the EPR measurements. The authors also would like to thank Professor Dr. Elson Longo for the use of BET facilities.

References and Notes

1. J. J. Spivey, *Ind. Eng. Chem. Res.* 26, 2165 (**1987**).
2. L. F. Liotta, *Applied Catalysis B-Environmental* 100, 403 (**2010**).
3. B. Solsona, T. E. Davies, T. Garcia, I. Vazquez, A. Dejoz, and S. H. Taylor, *Appl. Catal. B-Environ.* 84, 176 (**2008**).
4. S. C. Kim and W. G. Shim, *Applied Catalysis B-Environmental* 92, 429 (**2009**).
5. Z. Abbasi, M. Haghighi, E. Fatehifar, and S. Saedy, *J. Hazard Mater.* 186, 1445 (**2011**).
6. R. Balzer, V. Drago, W. H. Schreiner, and L. F. D. Probst, *J. Brazil Chem. Soc.* 24, 1592 (**2013**).
7. S. Todorova, G. Kadinov, K. Tenchev, A. Caballero, J. P. Holgado, and R. Pereniguez, *Catal. Lett.* 129, 149 (**2009**).
8. S. Azalim, M. Franco, R. Brahmi, J. M. Giraudon, and J. F. Lamonier, *J. Hazard. Mater.* 188, 422 (**2011**).
9. V. D. Araujo, M. M. de Lima, A. Cantarero, M. I. B. Bernardi, J. D. A. Bellido, E. M. Assaf, R. Balzer, L. F. D. Probst, and H. V. Fajardo, *Mater. Chem. Phys.* 142, 677 (**2013**).
10. A. S. K. Sinha and V. Shankar, *Ind. Eng. Chem. Res.* 32, 1061 (**1993**).
11. A. Berenjian, N. Chan, and H. J. Malmiri, *American Journal of Biochemistry and Biotechnology* 8, 220 (**2012**).
12. T. Ataloglou, C. Fountzoula, K. Bourikas, J. Vakros, A. Lycourghiotis, and C. Kordulis, *Applied Catalysis A-General* 288, 1 (**2005**).

13. B. Solsona, M. Perez-Cabero, I. Vazquez, A. Dejoz, T. Garcia, J. Alvarez-Rodriguez, J. El-Haskouri, D. Beltran, and P. Amoros, *Chem. Eng. J.* 187, 391 **(2012)**.
14. P. Papaefthimiou, T. Ioannides and X. E. Verykios, *Applied Catalysis B-Environmental* 13, 175 **(1997)**.
15. A. Szegedi, M. Popova, and C. Minchev, *Journal of Materials Science* 44, 6710 **(2009)**.
16. S. Ifrah, A. Kaddouri, P. Gelin, and D. Leonard, *Comptes Rendus Chimie.* 10, 1216 **(2007)**.
17. T. M. Milao, V. R. de Mendonca, V. D. Araujo, W. Avansi, C. Ribeiro, E. Longo, and M. I. Bernardi, *Science of Advanced Materials* 4, 54 **(2012)**.
18. S. Komarneni, *Current Science* 85, 1730 **(2003)**.
19. P. G. Mendes, M. L. Moreira, S. M. Tebcherani, M. O. Orlandi, J. Andres, M. S. Li, N. Diaz-Mora, J. A. Varela, and E. Longo, *J. Nanopart. Res.* 14 **(2012)**.
20. X. H. Yu, Y. C. Hu, L. Zhou, F. J. Cao, Y. X. Yang, T. Liang, and J. H. He, *Curr. Nanosci.* 7, 576 **(2011)**.
21. M. Fernandez-Garcia, A. Martinez-Arias, J. C. Hanson, and J. A. Rodriguez, *Chem. Rev.* 104, 4063 **(2004)**.
22. A. C. Larson and R. B. V. Dreele, In. Los Alamos National Laboratory Report LAUR 86 **(1994)**.
23. C. Y. Cao, Z. M. Cui, C. Q. Chen, W. G. Song, and W. Cai, *Journal of Physical Chemistry C* 114, 9865 **(2010)**.
24. V. D. Araujo, W. Avansi, H. B. de Carvalho, M. L. Moreira, E. Longo, C. Ribeiro, and M. I. B. Bernardi, *Crystengcomm.* 14, 1150 **(2012)**.
25. P. J. B. Marcos and D. Gouvêa, *Cerâmica* 50, 38 **(2004)**.
26. H. P. Klug and L. E. Alexander, X-ray Diffraction Procedures: For Polycrystalline and Amorphous Materials, Wiley-Interscience Publication, New York **(1974)**.
27. S. Kumar, Y. J. Kim, B. H. Koo, H. Choi, and C. G. Lee, *Ieee Transactions on Magnetics* 45, 2439 **(2009)**.
28. R. D. Shannon, *Acta Crystallographica Section A* 32, 751 **(1976)**.
29. J. E. Spanier, R. D. Robinson, F. Zheng, S. W. Chan, and I. P. Herman, *Physical Review B* 64 **(2001)**.
30. A. S. P. Lovon, J. J. Lovon-Quintana, G. I. Almerindo, G. P. Valenca, M. I. B. Bernardi, V. D. Araujo, T. S. Rodrigues, P. A. Robles-Dutenhefner, and H. V. Fajardo, *J. Power Sources* 216, 281 **(2012)**.
31. J. R. Mcbride, K. C. Hass, B. D. Poindexter, and W. H. Weber, *J. Appl. Phys.* 76, 2435 **(1994)**.
32. V. G. Hadjiev, M. N. Iliev, and I. V. Vergilov, *Journal of Physics C-Solid State Physics* 21, L199 **(1988)**.
33. Z. V. Popovic, Z. D. Dohcevic-Mitrovic, N. Paunovic, and M. Radovic, *Physical Review B* 85 **(2012)**.
34. L. Q. Jing, Y. C. Qu, B. Q. Wang, S. D. Li, B. J. Jiang, L. B. Yang, W. Fu, H. G. Fu, and J. Z. Sun, *Sol. Energy Mater. Sol. Cells* 90, 1773 **(2006)**.
35. C. L. Chai, S. Y. Yang, Z. K. Liu, M. Y. Liao, and N. F. Chen, *Chin. Sci. Bull.* 48, 1198 **(2003)**.
36. F. Dong, W. R. Zhao, and Z. B. Wu, *Nanotechnology* 19 **(2008)**.
37. J. H. Liang, Z. X. Deng, X. Jiang, F. L. Li, and Y. D. Li, *Inorg. Chem.* 41, 3602 **(2002)**.
38. C. W. Sun, H. Li, H. R. Zhang, Z. X. Wang, and L. Q. Chen, *Nanotechnology* 16, 1454 **(2005)**.
39. M. Godinho, C. Ribeiro, E. Longo, and E. R. Leite, *Cryst. Growth Des.* 8, 384 **(2008)**.
40. A. Popa, D. Toloman, O. Raita, A. R. Biris, G. Borodi, T. Mustafa, F. Watanabe, A. S. Biris, A. Darabont, and L. M. Giurgiu, *Central European Journal of Physics* 9, 1446 **(2011)**.
41. B. M. Weckhuysen, A. A. Verberckmoes, M. G. Uytterhoeven, F. E. Mabbs, D. Collison, E. de Boer, and R. A. Schoonheydt, *J. Phys. Chem. B* 104, 37 **(2000)**.
42. S. K. Misra, S. I. Andronenko, K. M. Reddy, J. Hays, and A. Punnoose, *J. Appl. Phys.* 99 **(2006)**.
43. J. G. McAlpin, Y. Surendranath, M. Dinca, T. A. Stich, S. A. Stoian, W. H. Casey, D. G. Nocera, and R. D. Britt, *J. Am. Chem. Soc.* 132, 6882 **(2010)**.
44. S. K. Hoffmann, J. Goslar, and S. Lijewski, *Appl. Magn. Reson.* 44, 817 **(2013)**.
45. J. Chess, G. Alanko, D. A. Tenne, C. B. Hanna, and A. Punnoose, *J. Appl. Phys.* 113 **(2013)**.
46. P. Ratnasamy, D. Srinivas, C. V. V. Satyanarayana, P. Manikandan, R. S. S. Kumaran, M. Sachin, and V. N. Shetti, *J. Catal.* 221, 455 **(2004)**.
47. C. X. Zhang, S. R. Li, M. S. Li, S. P. Wang, X. B. Ma, and J. L. Gong, *Aiche J.* 58, 516 **(2012)**.
48. J. C. S. Wu, Z. A. Lin, F. M. Tsai, and J. W. Pan, *Catal. Today* 63, 419 **(2000)**.
49. M. Kang, M. W. Song, and C. H. Lee, *Applied Catalysis a-General* 251, 143 **(2003)**.
50. C. W. Tang, C. C. Kuo, M. C. Kuo, C. B. Wang, and S. H. Chien, *Applied Catalysis a-General* 309, 37 **(2006)**.
51. J. Y. Luo, M. Meng, X. Li, X. G. Li, Y. Q. Zha, T. D. Hu, Y. N. Xie, and J. Zhang, *J. Catal.* 254, 310 **(2008)**.
52. Q. Y. Yan, X. Y. Li, Q. D. Zhao, and G. H. Chen, *J. Hazard. Mater.* 209, 385 **(2012)**.
53. S. Todorova, H. Kolev, J. P. Holgado, G. Kadinov, C. Bonev, R. Pereniguez, and A. Caballero, *Applied Catalysis B-Environmental* 94, 46 **(2010)**.
54. T. Warang, N. Patel, A. Santini, N. Bazzanella, A. Kale, and A. Miotello, *Appl. Catal. a-Gen.* 423, 21 **(2012)**.
55. I. I. Soykal, B. Bayram, H. Sohn, P. Gawade, J. T. Miller, and U. S. Ozkan, *Applied Catalysis a-General* 449, 47 **(2012)**.
56. G. B. Sun, K. Hidajat, X. S. Wu, and S. Kawi, *Applied Catalysis B-Environmental* 81, 303 **(2008)**.
57. L. F. Liotta, G. Di Carlo, G. Pantaleo, and G. Deganello, *Catal. Commun.* 6, 329 **(2005)**.
58. H. Song and U. S. Ozkan, *J. Catal.* 261, 66 **(2009)**.
59. H. C. Genuino, S. Dharmarathna, E. C. Njagi, M. C. Mei, and S. L. Suib, *Journal of Physical Chemistry C* 116, 12066 **(2012)**.
60. D. Terribile, A. Trovarelli, C. de Leitenburg, A. Primavera, and G. Dolcetti, *Catal. Today* 47, 133 **(1999)**.

ARTICLE